

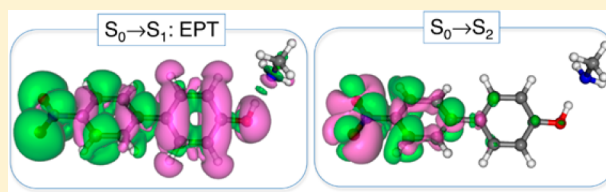
# Photoinduced Proton-Coupled Electron Transfer of Hydrogen-Bonded *p*-Nitrophenylphenol–Methylamine Complex in Solution

Chaehyuk Ko, Brian H. Solis, Alexander V. Soudackov, and Sharon Hammes-Schiffer\*

Department of Chemistry, 600 South Mathews Avenue, University of Illinois at Urbana–Champaign, Urbana, Illinois 61801, United States

## Supporting Information

**ABSTRACT:** Proton-coupled electron transfer can occur through concerted (electron–proton transfer, EPT) or sequential mechanisms, but this distinction becomes less well-defined for photoinduced reactions. These issues have been examined with transient absorption experiments on a hydrogen-bonded complex consisting of *p*-nitrophenylphenol and *t*-butylamine. These experiments revealed two spectroscopically distinct states: the higher-energy excited state was interpreted to be a conventional intramolecular charge transfer (ICT) state within the *p*-nitrophenylphenol, whereas the lower-energy state was interpreted to be an ICT-EPT state, where photoexcitation resulted in both ICT and the shifting of electronic density corresponding to effective proton transfer from the phenol to the amine. In the present work, the singlet excited states of the hydrogen-bonded *p*-nitrophenylphenol–methylamine complex in 1,2-dichloroethane are studied with time-dependent density functional theory and higher-level *ab initio* methods. The calculations suggest that the  $\pi\pi^*$  state, which is the  $S_1$  state at the Franck–Condon geometry, corresponds to the state denoted ICT-EPT in the experimental analysis, whereas the  $n\pi^*$  state, which is the  $S_2$  state at this geometry, likely corresponds to the state denoted ICT in the experimental analysis. According to the calculations, the  $\pi\pi^*$  state has charge-transfer character, as well as a change in electronic density on the amine, with the minimum-energy structure corresponding to the proton bonded to the nitrogen acceptor, consistent with proton transfer. The  $n\pi^*$  state has little charge-transfer character, as well as negligible change in electronic density on the amine, with the minimum-energy structure corresponding to the proton bonded to the oxygen donor. The calculations also provide evidence of an avoided crossing between these two states located energetically close to the Franck–Condon point. These calculations provide the foundation for future nonadiabatic molecular dynamics studies of the relaxation process.



## 1. INTRODUCTION

Proton-coupled electron transfer (PCET) reactions play a central role in many chemical and biological processes, including natural and artificial photosynthesis,<sup>1–5</sup> the catalytic oxidation and production of molecular hydrogen,<sup>6,7</sup> ultrafast relaxation of UV-radiated DNA systems,<sup>8–10</sup> and various enzyme reactions.<sup>11,12</sup> In general, PCET mechanisms can be sequential, with either the electron or proton transferring first, or concerted (electron–proton transfer, EPT), with the electron and proton transferring simultaneously.<sup>13</sup> Typically, sequential PCET mechanisms are defined in terms of the existence of a stable intermediate, although the rigorous definition of such an intermediate is not straightforward. Several definitions of a stable intermediate have been proposed, but these definitions tend to be rather subjective, such as the intermediate having a specified lifetime or being detectable with a particular experimental technique. From a theoretical perspective, a standard definition is that the intermediate corresponds to a minimum on the potential energy surface, but this property can depend on the particular level of theory. Furthermore, these definitions become even less well-defined for photoexcited PCET reactions, which are inherently nonequilibrium processes that are unlikely to exhibit equi-

brated intermediates during the ultrafast dynamics following photoexcitation. These mechanistic issues can be examined using ultrafast time-resolved spectroscopic methods to probe the nonequilibrium dynamics of photoinduced PCET processes.<sup>14–19</sup>

Recently, a spectroscopic study of photoinduced PCET in hydrogen-bonded dye molecules provided an unprecedented level of detailed dynamical information.<sup>20</sup> One of the systems studied was the hydrogen-bonded complex composed of *p*-nitrophenylphenol and *t*-butylamine, as depicted schematically in Figure 1, with methylamine replacing *t*-butylamine as the base. Femtosecond transient absorption spectra of this species

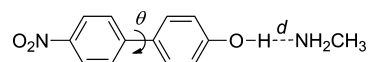


**Figure 1.** Hydrogen-bonded *p*-nitrophenylphenol–methylamine complex studied theoretically in the present work. In the experimentally studied system, the methylamine was replaced with *t*-butylamine.

**Received:** October 30, 2012

**Revised:** December 7, 2012

**Published:** December 13, 2012

in 1,2-dichloroethane revealed two spectroscopically distinct states with different dynamical behavior. Both states were interpreted as intramolecular charge transfer (ICT) states, in which an electron from a nonbonding orbital on the oxygen was transferred to the nitro group, forming an  $n\pi^*$  charge-transfer state. The shifting of electron density away from the oxygen was proposed to decrease the strength of the O–H bond, leading to proton transfer (PT) from the oxygen to the nitrogen of the hydrogen-bonded base. One of the excited states was interpreted to be a conventional ICT state, where the proton remained bonded to the donor oxygen and subsequently transferred to the acceptor nitrogen on the picosecond time scale. The other excited state was interpreted to be an ICT-EPT state, where photoexcitation resulted in the shifting of electronic density from the O–H bond to the N–H bond concurrently with ICT. According to the Franck–Condon (FC) principle, an electronic excitation occurs on a much faster time scale than nuclear rearrangement. Thus, the transferring hydrogen nucleus was assumed to remain fixed during the optical excitation, forming a highly elongated N–H bond that subsequently relaxed to equilibrium.

The transient absorption spectra exhibited both singlet and triplet bands with absorptions that depended on the excitation wavelength. In the present work, we focus on the singlet states that are populated at early times. For convenience, we adopt the ICT and ICT-EPT notation used to describe these states in ref 20. These two states were characterized by comparison of the absorption bands to those obtained for the free phenol and for the phenol hydrogen-bonded to a series of bases spanning a range of  $pK_a$  values. Analysis of the spectra observed 1 ps after photoexcitation indicated that both states are populated by 355-nm excitation but only the ICT-EPT state is populated by 388-nm excitation, suggesting that the ICT-EPT state is lower in energy at the ground-state equilibrium geometry (i.e., at the FC geometry). The ICT-EPT signature was present at the earliest observable pump–probe delay time of 200 fs, but the transient absorption experiments could not be used to rule out an ultrafast delayed PT occurring during this initial 200 fs. Coherent Raman measurements provided direct evidence of an elongated N–H bond in the excited state at the FC geometry.<sup>20</sup>

In the present work, we characterize the two experimentally relevant singlet excited states of the hydrogen-bonded *p*-nitrophenylphenol–methylamine complex in 1,2-dichloroethane. For this purpose, we use time-dependent density functional theory (TDDFT)<sup>21</sup> with long-range corrected functionals in conjunction with the polarizable continuum model (PCM)<sup>22</sup> for solvation. We benchmark this methodology by comparison to higher-level *ab initio* methods. Our objective is to analyze the electronic structure of the two relevant low-lying singlet excited states at the equilibrium ground-state geometry and to probe the potential energy surfaces of these two excited states in the vicinity of the FC geometry. Although we do not perform any dynamical calculations or generate vibrational spectra, we interpret the results qualitatively in the context of the transient absorption and coherent Raman experiments. Our results are consistent with the experimental data and provide additional insights into the nature of the singlet excited states. The  $S_1$  state exhibits one or two minima, depending on the level of theory, with the lowest-energy minimum corresponding to the proton bonded to the acceptor, consistent with PT. The  $S_2$  state exhibits only one minimum associated with the proton bonded to the donor, corresponding to a structure similar to the FC geometry.

According to our calculations, however, the  $S_1$  state is characterized as a  $\pi\pi^*$  transition with charge-transfer character, and the  $S_2$  state is characterized as an  $n\pi^*$  transition with little charge-transfer character.

An outline of the article is as follows. Section 2 briefly summarizes the computational methodology. Section 3 presents and discusses the results, starting with calculations of the vertical excitation energies, followed by the generation of approximate potential energy surfaces as functions of the relevant nuclear coordinates. The last part of this section analyzes the relation of the results to the dynamics observed experimentally. Concluding remarks are provided in section 4.

## 2. COMPUTATIONAL METHODS

Despite the known limitations of TDDFT for correctly describing doubly excited states and conical intersections, the geometries and energetics of singly excited low-lying valence states obtained with TDDFT have been shown to be in good agreement with multireference perturbation theory (CASPT2) results.<sup>23</sup> In the present work, we used TDDFT to calculate vertical excitation energies and generate approximate potential energy surfaces. We did not attempt to optimize conical intersections, although we located avoided crossing regions between the  $S_1$  and  $S_2$  states. As photoinduced PCET reactions involve excited states of charge-transfer character, long-range corrected density functionals, specifically CAM-B3LYP,<sup>24</sup> LC- $\omega$ PBE,<sup>25–27</sup> and  $\omega$ B97XD,<sup>28</sup> were used. For benchmarking purposes, we also performed *ab initio* calculations with EOM-CCSD,<sup>29,30</sup> CIS(D),<sup>31</sup> and CASPT2<sup>32</sup> for certain cases. All results presented in the tables and figures in the main text were obtained with the 6-31G(d) basis set unless otherwise specified. Results obtained with the 6-31+G(d,p) basis set are provided in the Supporting Information. Moreover, all calculations were performed using Gaussian 09,<sup>33</sup> except for the CASPT2 calculations, which were performed using MOLCAS.<sup>34</sup>

The solvent was described with PCM using the defaults in Gaussian 09. To be consistent with the experiments, the solvent was chosen to be 1,2-dichloroethane, which has dielectric constants of  $\epsilon_0 = 10.1$  and  $\epsilon_\infty = 2.1$ . For calculations of the vertical excitation energies at the FC geometry, we used nonequilibrium PCM solvation, where only the solvent electronic polarization (i.e., the fast degrees of freedom) is in equilibrium with the excited-state electronic density. For optimizing excited-state geometries to generate the potential energy surfaces, we used equilibrium PCM solvation, where the solvent electronic and nuclear polarizations (i.e., the fast and slow degrees of freedom) are in equilibrium with the excited-state electronic density.

Both linear-response (LR) PCM<sup>35</sup> and state-specific (SS) PCM<sup>36,37</sup> calculations were performed. Previous studies have shown that LR-PCM-TDDFT provides a reliable treatment of solvation effects in electronic transitions with large oscillator strengths and provides physically reasonable excited-state geometries.<sup>38–40</sup> In SS-PCM-TDDFT, the solvent polarization field and the charge density of a specific excited state are determined self-consistently, leading to a more balanced description of solvent effects for different excited states. For the calculation of vertical excitation energies, nonequilibrium LR-PCM-TDDFT was used for all systems studied, and nonequilibrium SS-PCM-TDDFT was used only for the cases where specified. For the generation of the potential energy surfaces, the excited-state geometries were optimized using equilibrium LR-PCM-TDDFT,<sup>41</sup> and equilibrium SS-PCM-

**Table 1. Vertical Excitation Energies ( $E_{\text{exc}}$ , eV), Oscillator Strengths ( $f$ ), and Dipole Moment Magnitudes ( $|\mu|$ , Debye) at the Ground-State Equilibrium Geometry of *p*-Nitrophenylphenol in the Gas Phase<sup>a</sup>**

	EOM-CCSD <sup>b</sup>		CASPT2 <sup>b,c</sup>		CIS(D) <sup>b</sup>	
	$E_{\text{exc}}$	$f$	$E_{\text{exc}}$	$f^d$	$E_{\text{exc}}$	$f^e$
S <sub>1</sub>	3.98	0.0004	3.92	0.0009	3.76	0.0031
S <sub>2</sub>	4.50	0.0001	4.39	0.0001	4.45	0.0002
S <sub>3</sub>	4.88	0.0032	4.83	0.0176	4.89	0.0162
S <sub>4</sub>	4.97	0.0112	5.17	0.5145	5.00	0.0252
S <sub>5</sub>	4.99	0.6942	6.29	0.0127	5.03	0.7158
S <sub>6</sub>	6.16	0.0005			6.45	0.0006

	LC- $\omega$ PBE <sup>f,g</sup>		$\omega$ B97XD <sup>f</sup>			CAM-B3LYP <sup>f</sup>		
	$E_{\text{exc}}$	$f$	$E_{\text{exc}}$	$f$	$ \mu $	$E_{\text{exc}}$	$f$	$ \mu $
S <sub>1</sub>	3.71	0.0075	3.79	0.0133	4.1	4.00	0.0021	3.8
S <sub>2</sub>	4.21	0.0000	4.28	0.0001	4.2	4.41	0.5986	16.0
S <sub>3</sub>	4.73	0.5930	4.56	0.5401	15.6	4.51	0.0001	4.1
S <sub>4</sub>	4.93	0.0064	4.83	0.0095	9.3	4.91	0.0096	8.8
S <sub>5</sub>	5.09	0.0228	5.14	0.0197	6.7	5.13	0.0106	7.0
S <sub>6</sub>	5.71	0.0029	5.58	0.0014	13.8	5.71	0.0010	12.4

<sup>a</sup>6-31G(d) basis set used for all calculations in this table. <sup>b</sup>Ground-state geometry optimization performed with MP2. <sup>c</sup>Reference CASSCF wave function has 14 electrons and 11 orbitals in the active space and was averaged over six states with equal weights. <sup>d</sup>Oscillator strength obtained from CASSCF reference wave function. <sup>e</sup>Oscillator strength obtained from CIS reference wave function. <sup>f</sup>Ground-state geometry optimization performed with DFT using the specified functional. <sup>g</sup>Dipole moments were not calculated because the analytic third derivatives of the LC- $\omega$ PBE functional are not currently implemented in Gaussian 09. The range partitioning parameter,  $\omega$ , was set to 0.3.

**Table 2. Vertical Excitation Energies ( $E_{\text{exc}}$ , eV), Oscillator Strengths ( $f$ ), and Dipole Moment Magnitudes ( $|\mu|$ , Debye) at the Ground-State Equilibrium Geometry of *p*-Nitrophenylphenol in 1,2-Dichloroethane<sup>a</sup>**

	CASPT2 <sup>b</sup>		LC- $\omega$ PBE <sup>c,d</sup>		$\omega$ B97XD <sup>c</sup>			CAM-B3LYP <sup>c</sup>		
	$E_{\text{exc}}$	$f^e$	$E_{\text{exc}}$	$f$	$E_{\text{exc}}$	$f$	$ \mu $	$E_{\text{exc}}$	$f$	$ \mu $
S <sub>1</sub>	3.96	0.0000	3.93	0.0018	4.03	0.0217	5.9	4.01	0.1085	8.6
S <sub>2</sub>	4.50	0.0181	4.43	0.7765	4.22	0.7233	18.0	4.09	0.6033	16.5
S <sub>3</sub>	4.55	0.0001	4.48	0.0001	4.59	0.0001	5.0	4.59	0.0001	5.0
S <sub>4</sub>	4.90	0.5327	4.86	0.0159	4.73	0.0189	11.5	4.74	0.0182	11.4
S <sub>5</sub>	6.16	0.0165	5.08	0.0204	5.11	0.0139	8.7	5.08	0.0083	10.0

<sup>a</sup>6-31G(d) basis set used for all calculations in this table. <sup>b</sup>Ground-state geometry optimization performed with MP2 and PCM solvation. Reference CASSCF wave function has 14 electrons and 11 orbitals in the active space and was averaged over six states with equal weights. <sup>c</sup>Ground-state geometry optimization performed with DFT using the specified functional with PCM solvation. Excited-state properties calculated with nonequilibrium linear response PCM. <sup>d</sup>Dipole moments were not calculated because the analytic third derivatives of the LC- $\omega$ PBE functional are not currently implemented in Gaussian 09. The range partitioning parameter,  $\omega$ , was set to 0.3. <sup>e</sup>Oscillator strength obtained from CASSCF reference wave function.

**Table 3. Vertical Excitation Energies ( $E_{\text{exc}}$ , eV), Oscillator Strengths ( $f$ ), and Dipole Moment Magnitudes ( $|\mu|$ , Debye) at the Ground-State Equilibrium Geometry of the *p*-Nitrophenylphenol–Methylamine Hydrogen-Bonded Complex in 1,2-Dichloroethane<sup>a</sup>**

	CASPT2 <sup>b</sup>		LC- $\omega$ PBE <sup>c,d</sup>		$\omega$ B97XD <sup>c</sup>			CAM-B3LYP <sup>c</sup>		
	$E_{\text{exc}}$	$f^e$	$E_{\text{exc}}$	$f$	$E_{\text{exc}}$	$f$	$ \mu $	$E_{\text{exc}}$	$f$	$ \mu $
S <sub>1</sub>	3.98	0.0005	3.93	0.0156	3.94	0.8014	23.0	3.77	0.8342	25.9
					3.46			3.21		
S <sub>2</sub>	4.28	0.0002	4.14	0.9230	4.04	0.0817	9.5	4.03	0.0126	8.8
S <sub>3</sub>	4.59	0.5963	4.48	0.0001	4.59	0.0001	8.8	4.59	0.0001	9.2
S <sub>4</sub>			4.83	0.0268	4.70	0.0276	15.1	4.70	0.0264	15.4
S <sub>5</sub>			4.94	0.0391	4.98	0.0333	12.3	4.96	0.0188	14.0

<sup>a</sup>6-31G(d) basis set used for all calculations in this table. See Table S1 (Supporting Information) for the TDDFT results with the  $\omega$ B97XD and CAM-B3LYP functionals in conjunction with larger basis sets. <sup>b</sup>Ground-state geometry optimization performed with MP2 and PCM solvation. Reference CASSCF wave function has 14 electrons and 11 orbitals in the active space and was averaged over six states with equal weights. <sup>c</sup>Ground-state geometry optimization performed with DFT using the specified functional with PCM solvation. Excited-state properties calculated with nonequilibrium linear response PCM except for excitation energies in italics, which were calculated with nonequilibrium state-specific PCM. <sup>d</sup>Dipole moments were not calculated because the analytic third derivatives of the LC- $\omega$ PBE functional are not currently implemented in Gaussian 09. The range partitioning parameter,  $\omega$ , was set to 0.3. <sup>e</sup>Oscillator strength obtained from CASSCF reference wave function.



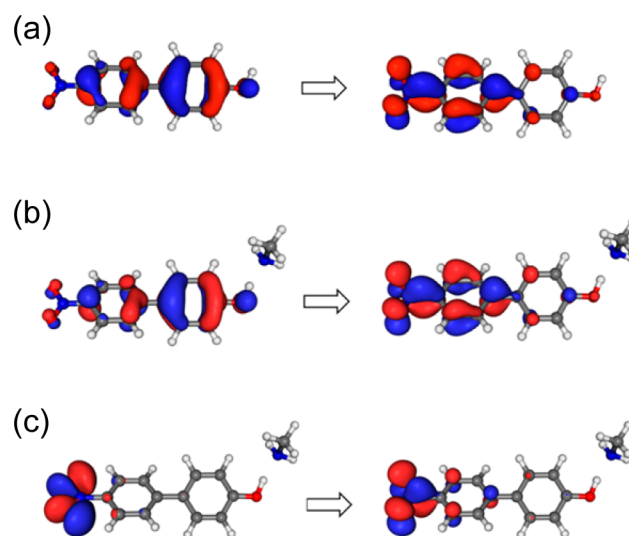
TDDFT calculations were performed at some of these geometries.

### 3. RESULTS AND DISCUSSION

**3.1. Vertical Excitation Energies.** Tables 1–3 present the calculated vertical excitation energies for the low-lying singlet states of *p*-nitrophenylphenol in the gas phase, *p*-nitrophenylphenol in solution, and the hydrogen-bonded *p*-nitrophenylphenol–methylamine complex in solution, respectively. The ground-state geometries were optimized with MP2 for the EOM-CCSD, CIS(D), and CASPT2 calculations and with DFT using the specified functional for the TDDFT calculations. In Table 1, which presents gas-phase results, the systems were optimized in the gas phase, and in Tables 2 and 3, which present solution-phase results, the systems were optimized with PCM. For the CASPT2 calculations, the CASSCF reference wave function was averaged over six equally weighted states with 14 electrons and 11 orbitals in the active space, and the multistate CASPT2<sup>42</sup> implemented in MOLCAS<sup>34</sup> was used. For the hydrogen-bonded *p*-nitrophenylphenol–methylamine complex, we did not include corrections for the basis set superposition error (BSSE), which could potentially lead to underestimation of the donor–acceptor distance.<sup>43</sup> Although a large basis set is required to reduce the BSSE significantly for wave function methods, the BSSE tends to be less pronounced for DFT, especially when diffuse functions are included in the basis sets.<sup>44</sup> As mentioned in the previous section, most of the results presented in the main text were performed with the 6-31G(d) basis set, but the results using a larger basis set including diffuse basis functions are given in the Supporting Information. The basis set without diffuse basis functions was found to provide qualitatively similar results for the solvated systems studied here.

As indicated by Table 1, the first bright state for *p*-nitrophenylphenol in the gas phase is  $S_5$  for EOM-CCSD and CIS(D),  $S_4$  for CASPT2,  $S_3$  for TDDFT with the LC- $\omega$ PBE and  $\omega$ B97XD functionals, and  $S_2$  for TDDFT/CAM-B3LYP. Although the state ordering is not the same among the different methods and the TDDFT method leads to somewhat lower vertical excitation energies, all of the methods are in agreement that the dominant transition for the bright state is of  $\pi\pi^*$  type with charge-transfer character. Note that the dipole moment of the ground state at the equilibrium geometry obtained with DFT/CAM-B3LYP is 5.9 D, and the dipole moment of the first bright state obtained with TDDFT/CAM-B3LYP is  $\sim 16$  D, indicating charge-transfer character of this transition. The TDDFT/CAM-B3LYP orbitals representing the dominant transition associated with the bright state are depicted in Figure 2a. The corresponding orbitals obtained from the other methods are provided in the Supporting Information.

The vertical excitation energies for *p*-nitrophenylphenol in solution are given in Table 2. The bright state with charge-transfer character for this system is  $S_2$  for TDDFT with all three functionals and  $S_4$  for CASPT2. Although the state ordering differs for TDDFT and CASPT2, the character of the bright state is very similar. Specifically, the bright state is of  $\pi\pi^*$  type with charge-transfer character, as in the gas phase. In addition, the vertical excitation energy is  $\sim 0.3$  eV lower in solution than in the gas phase for all of these methods. The experimental absorption maximum for *p*-nitrophenylphenol in solution is  $\sim 3.7$  eV, so all of these methods slightly overestimate the vertical excitation energy.<sup>20</sup>



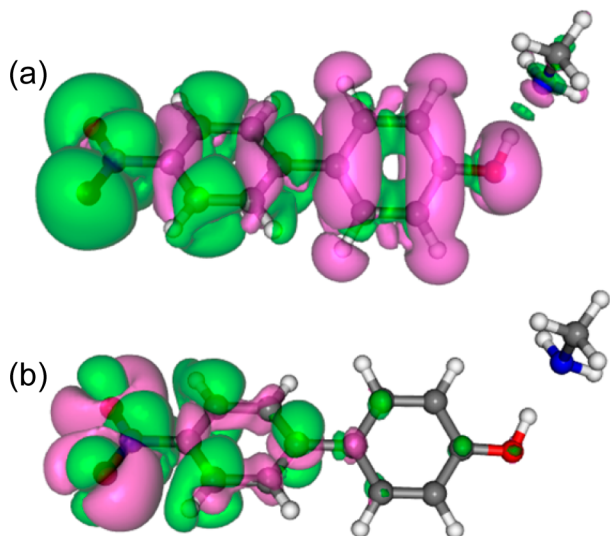
**Figure 2.** Natural transition orbitals representing the dominant transitions of (a)  $S_2$  of *p*-nitrophenylphenol in the gas phase, (b)  $S_1$  of the *p*-nitrophenylphenol–methylamine complex in solution, and (c)  $S_2$  of the *p*-nitrophenylphenol–methylamine complex in solution. These orbitals were obtained with the nonequilibrium LR-PCM TDDFT/CAM-B3LYP/6-31G(d) method at the ground-state equilibrium geometries. The natural transition orbitals represent more than 97% of the transition matrix for each state. Transitions a and b lead to the bright excited state in the gas-phase and solvated systems, respectively. See Figures S1–S9 (Supporting Information) for these and other natural transition orbitals obtained at various levels of theory.

Table 3 presents the vertical excitation energies for the hydrogen-bonded *p*-nitrophenylphenol–methylamine complex in solution. In this case, the bright state is  $S_1$  for TDDFT with the  $\omega$ B97XD and CAM-B3LYP functionals,  $S_2$  for TDDFT/LC- $\omega$ PBE, and  $S_3$  for CASPT2. The experimental absorption maximum for the complex with *t*-butylamine in solution is  $\sim 3.5$  eV. Although the calculated vertical excitation energies vary among the different methods, the calculated red shifts upon complex formation are 0.2–0.3 eV, in good agreement with the experimentally observed shift of 0.2 eV. For TDDFT with the  $\omega$ B97XD and CAM-B3LYP functionals, the nonequilibrium SS-PCM-TDDFT results for the bright states are shown in *italics*. These vertical excitation energies are  $\sim 0.5$  eV lower with the SS-PCM than with the LR-PCM solvation method.

Both the  $\omega$ B97XD and CAM-B3LYP functionals predict  $S_1$  to be the bright state for the hydrogen-bonded complex in solution, and the calculated vertical excitation energies are in qualitative agreement with the experimental results (i.e., within 0.3–0.5 eV). Moreover, both functionals show that  $S_2$  is somewhat bright, although with significantly lower oscillator strength than the  $S_1$  state. The characters of the  $S_1$  and  $S_2$  states obtained with these two functionals are very similar. In particular,  $S_1$  is a  $\pi\pi^*$  state with charge-transfer character, and  $S_2$  is an  $n\pi^*$  state without significant charge-transfer character, based on the calculated dipole moments. Panels b and c of Figure 2 depict the TDDFT/CAM-B3LYP orbitals representing the dominant transitions of the bright  $\pi\pi^*$  state and close-lying  $n\pi^*$  state, respectively, for the hydrogen-bonded complex in solution. The corresponding orbitals obtained with the  $\omega$ B97XD functional are virtually identical, as illustrated in Figure S7 of the Supporting Information.

As discussed further below, we associate the  $S_1$  and  $S_2$  states with the ICT-EPT and ICT states, respectively, discussed in the

Introduction, even though this terminology might not be applicable because the higher state does not exhibit significant charge-transfer character. Based on the experimental analysis, an excitation of 3.2 eV populates the ICT-EPT state, and an excitation of 3.5 eV populates both the ICT and ICT-EPT states. These relative excitation energies are qualitatively consistent with the calculated vertical excitation energies for the  $S_1$  and  $S_2$  states. Moreover, Figure 3, which depicts the



**Figure 3.** Isosurfaces of electronic density differences between the lowest-lying singlet excited states and the ground state of the *p*-nitrophenylphenol–methylamine complex in solution at the ground-state equilibrium geometry. The electronic density differences corresponding to the (a)  $S_0 \rightarrow S_1$  and (b)  $S_0 \rightarrow S_2$  transitions are depicted. The electronic densities were obtained with the PCM DFT/CAM-B3LYP/6-31G(d) method for the ground state and the nonequilibrium LR-PCM TDDFT/CAM-B3LYP/6-31G(d) method for the excited states. The isosurfaces of 0.0005 and  $-0.0005 \text{ Bohr}^{-3}$  are depicted in green and magenta, respectively. Note that a change in the electronic density on the amine base accompanies the optical excitation to  $S_1$  but not to  $S_2$ .

difference in electronic density for the transitions  $S_0 \rightarrow S_1$  and  $S_0 \rightarrow S_2$ , illustrates that a change in the electronic density on the amine base accompanies the optical excitation to  $S_1$  but not to  $S_2$ . As discussed previously, according to the interpretation of the experiments, photoexcitation to the ICT-EPT state shifts the electronic density from the O–H bond to the N–H bond concurrently with ICT. Thus, the observed change in electronic density on the amine upon excitation to  $S_1$ , in conjunction with the absence of such a change upon excitation to  $S_2$ , is consistent with the assignment of the  $S_1$  state as the ICT-EPT state and the  $S_2$  state as the ICT state.

**3.2. Approximate Potential Energy Surfaces.** We found that the  $\omega$ B97XD and CAM-B3LYP functionals yield similar results in terms of the geometries and energetics of the two low-lying singlet excited states. In this subsection, the TDDFT/CAM-B3LYP results are presented. The analogous TDDFT/ $\omega$ B97XD results are presented in the Supporting Information. To characterize the  $S_1$  and  $S_2$  excited states, the geometries of these two excited states were optimized with the equilibrium LR-PCM-TDDFT approach. Figure 4 depicts the resulting equilibrium geometries.

We located two minima for the  $\pi\pi^*$  state, which is the  $S_1$  state at the FC point. In both minimum-energy geometries, the

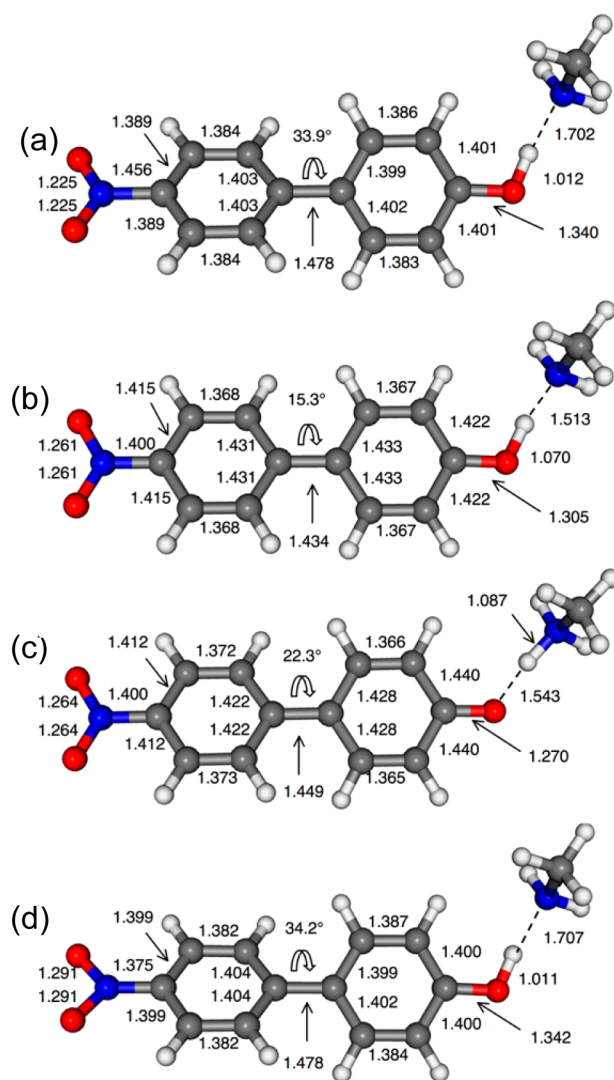


**Figure 4.** Equilibrium geometries of the *p*-nitrophenylphenol–methylamine complex in solution optimized using the equilibrium LR-PCM TDDFT/CAM-B3LYP/6-31G(d) method. The bond lengths are given in angstroms. (a) Ground-state equilibrium geometry, (b)  $\pi\pi^*$  excited-state equilibrium geometry with the transferring proton bonded to the donor oxygen atom (denoted D in the text), (c)  $\pi\pi^*$  excited-state equilibrium geometry with the transferring proton bonded to the acceptor nitrogen atom (denoted A in the text), (d)  $n\pi^*$  excited-state equilibrium geometry. See Figure S10 (Supporting Information) for the analogous figure generated with the  $\omega$ B97XD functional and Figures S11 and S12 (Supporting Information) for these geometries obtained at various levels of theory.

bond length pattern of the rings is quinoidal, as in the ICT state of 4-(dimethyl)aminobenzonitrile (DMABN).<sup>45</sup> The main difference between the two minimum-energy structures is the position of the transferring proton of the phenol group. The geometry in Figure 4b, denoted as D hereafter, has the proton bonded to the donor oxygen, whereas the geometry in Figure 4c, denoted as A hereafter, has the proton bonded to the acceptor nitrogen. The A minimum is lower in energy than the D minimum by  $\sim 0.1 \text{ eV}$ .

On the basis of the state ordering at the FC geometry, the charge-transfer character, and the lowest-energy equilibrium geometry corresponding to PT to the nitrogen, we assign the  $\pi\pi^*$  state as the ICT-EPT state observed experimentally.

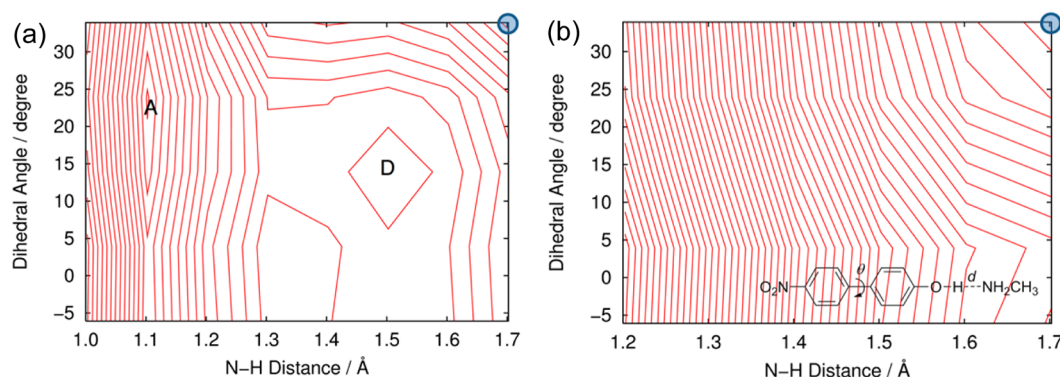


**Figure 5.** Potential energy surfaces of the (a)  $\pi\pi^*$  and (b)  $n\pi^*$  excited states of the *p*-nitrophenylphenol–methylamine complex in solution. For given values of the dihedral angle  $\theta$  and N–H distance  $d$  (see the inset), the other nuclear coordinates were optimized for each state using the equilibrium LR-PCM TDDFT/CAM-B3LYP/6-31G(d) method. Both surfaces correspond to the lowest-energy singlet excited state at each optimized geometry for given values of  $\theta$  and  $d$ . The shaded circles denote the FC geometry. The contour interval is 0.25 mHartree. The molecular geometries corresponding to minima D and A on the  $\pi\pi^*$  surface are depicted in panels b and c, respectively, of Figure 4. The minimum on the  $n\pi^*$  surface is very close to the FC geometry, with the geometrical differences localized around the nitro group, as illustrated in Figure 4d. See Figure S13 (Supporting Information) for the analogue to panel a generated with the 6-31+G(d,p) basis set; with this larger basis set, the D minimum is not located.

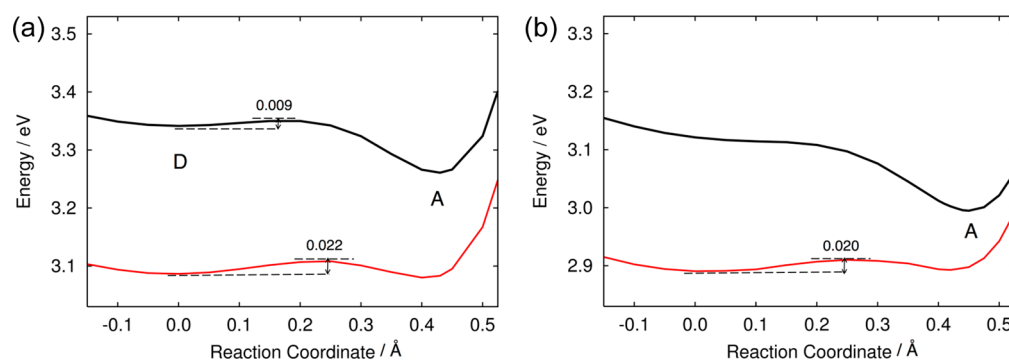


**Figure 6.** Pathway along a predominantly proton-transfer reaction coordinate on the  $\pi\pi^*$  excited-state potential energy surface of the *p*-nitrophenylphenol–methylamine complex in solution. For each fixed N–H distance  $d$ , all other nuclear coordinates were optimized on the  $\pi\pi^*$  state using the equilibrium LR-PCM TDDFT/CAM-B3LYP method. The black lines correspond to the LR-PCM TDDFT energies, and the red lines correspond to the SS-PCM TDDFT energies at the same geometries. These curves were generated with two different basis sets: (a) 6-31G(d) and (b) 6-31+G(d,p). Note that only the A minimum is located with CAM-B3LYP/6-31+G(d,p). The energy is given relative to the ground-state energy at the FC geometry for each level of theory. See Figure S19 (Supporting Information) for the analogous figures obtained using the  $\omega$ B97XD functional.

Previously, the ICT states in this system were proposed to arise from the electronic transition from the nonbonding orbital of the donor oxygen atom to a  $\pi^*$  orbital of the nitro group.<sup>20</sup> Our calculations are not consistent with this previous interpretation. The optimized structures of D and A indicate that the quinoidal structure arising from the  $\pi\pi^*$  transition (Figure 2b) decreases the C–O bond length of the phenol, thereby effectively increasing its acidity.

For the  $n\pi^*$  state, which is the  $S_2$  state at the FC geometry, we located only a single minimum. Note that the  $n\pi^*$  state is  $S_1$  at the corresponding optimized geometry shown in Figure 4d. The geometrical changes from the FC point to the  $n\pi^*$  minimum are localized around the nitro group, as suggested by the nature of the  $\pi^*$  orbital depicted on the right side of Figure 2c. This orbital exhibits strong antibonding character between the nitrogen atom and the two oxygen atoms in the nitro group, along with enhanced bonding character between the nitrogen atom and the carbon atom of the phenyl ring. The bond length pattern of the  $n\pi^*$  equilibrium geometry depicted in Figure 4d clearly reflects these characteristics in the region around the nitro group. The bond lengths of the rest of the  $n\pi^*$

equilibrium geometry are similar to those of the ground-state equilibrium geometry depicted in Figure 4a. In both cases, PT from the phenol to the base is not favored.

On the basis of the state ordering at the FC point and the existence of only a single minimum with the proton bonded to the phenol, we assign the  $n\pi^*$  state to the state that was denoted ICT in the interpretation of the experiments. The magnitude of the dipole moment of this state at the FC geometry, however, is estimated to be  $\sim 9$  D (Table 3), which is slightly smaller than the ground-state value of 11.2 D at the DFT/CAM-B3LYP level. In addition, the  $n\pi^*$  transition is largely localized in the nitrophenyl group. Thus, the  $n\pi^*$  state does not appear to have significant charge-transfer character, and the ICT label might not be applicable for this state.

We generated the potential energy surfaces in the regions around the FC point and excited-state minima as functions of the distance between the transferring proton and the nitrogen acceptor ( $d$  in Figure 1) and the dihedral angle around the bridging bond between the two rings ( $\theta$  in Figure 1). At each value of the H–N distance and the dihedral angle, the other nuclear coordinates were optimized on a specified state (i.e., the



$\pi\pi^*$  or  $n\pi^*$  state) using equilibrium LR-PCM-TDDFT/CAM-B3LYP. The resulting contour plots are depicted in Figure 5. The FC geometry is identified with the blue circle. As expected, two possible relaxation channels from the FC geometry to the **D** and **A** minima are found on the  $\pi\pi^*$  surface. The minima **D** and **A** are separated by a small barrier of 0.009 eV, with the **A** minimum lower than the **D** minimum by  $\sim 0.1$  eV. In contrast, only a single minimum is found on the  $n\pi^*$  surface, and the FC geometry is virtually identical to this minimum on the two-dimensional surface (i.e.,  $d$  and  $\theta$  are very similar in Figure 4a,d). We emphasize that these two-dimensional potential energy surfaces assume that all other solute degrees of freedom and the solvent respond instantaneously to changes in the  $d$  and  $\theta$  coordinates and therefore do not provide direct information about the nonequilibrium dynamics following photoexcitation. Nevertheless, these equilibrium potential energy surfaces provide qualitative information about the nature of these two excited electronic states.

Figure 6 depicts the reaction pathway as a function of the N–H distance  $d$  for the  $\pi\pi^*$  state. The geometries were obtained by fixing the N–H distance to specified values and optimizing all other solute coordinates with equilibrium LR-PCM-TDDFT. In Figure 6, the black lines represent the equilibrium LR-PCM-TDDFT energies, whereas the red lines represent the equilibrium SS-PCM-TDDFT energies for the geometries used to generate the black lines. The plots in panels a and b of Figure 6 were obtained using CAM-B3LYP/6-31G(d) and CAM-B3LYP/6-31+G(d,p), respectively. The analogous figures obtained using the  $\omega$ B97XD functional are depicted in Figure S19 (Supporting Information). For the 6-31G(d) basis set, the CAM-B3LYP and  $\omega$ B97XD functionals give similar barriers, with the CAM-B3LYP functional giving a slightly lower barrier. Increasing the size of the basis set tends to lower this barrier. As shown in Figure S19 (Supporting Information) for the  $\omega$ B97XD functional, addition of diffuse functions on the hydrogen atoms [i.e., the 6-31++G(d,p) basis set] leads to virtually identical results to those obtained with the 6-31+G(d,p) basis set. For LR-PCM-TDDFT/CAM-B3LYP/6-31+G(d,p) optimizations, only the **A** minimum is located on the  $\pi\pi^*$  state, as shown in Figure 6b and the two-dimensional surface depicted in Figure S13 (Supporting Information), the analogue of Figure 5a with the larger basis set. Note that these energy barriers might be underestimated because of the known limitations of DFT<sup>44</sup> and the use of equilibrium PCM solvation. In general, these levels of theory cannot distinguish between PT with a very small barrier and barrierless PT.

We also generated the two-dimensional potential energy surfaces with SS-PCM-TDDFT for the geometries generated with LR-PCM-TDDFT optimizations (i.e., for the geometries used to generate the surfaces in Figure 5). The SS-PCM-TDDFT  $n\pi^*$  potential energy surface is provided in Figure S14 (Supporting Information) and is qualitatively similar to the LR-PCM-TDDFT surface shown in Figure 5b. The SS-PCM-TDDFT  $\pi\pi^*$  potential energy surface indicated that the two minima were located at larger dihedral angles near  $90^\circ$ . To further explore these surfaces, we generated the  $\pi\pi^*$  surfaces with a two-dimensional rigid scan along  $\theta$  and  $d$ , where only those two internal coordinates were changed and all other internal coordinates were fixed to the values at the FC geometry. Figures S15–S18 (Supporting Information) depict the rigid scans obtained with LR-PCM-TDDFT and SS-PCM-TDDFT with both the 6-31G(d) and 6-31+G(d,p) basis sets.

In contrast to the barrierless relaxation from the FC geometry to the **A** minimum exhibited in the LR-PCM-TDDFT surface depicted in Figure 5a, the analogous rigid scan depicted in Figure S15 (Supporting Information) exhibits a barrier from the FC geometry to the **A** geometry. This barrier suggests that relaxation of the other solute degrees of freedom is necessary, as also indicated by the quinoidal structure of the optimized geometry in this excited state (Figure 4c).

Comparison of Figures S15 and S17 (Supporting Information) indicates that the rigid-scan  $\pi\pi^*$  surfaces obtained with SS-PCM-TDDFT and LR-PCM-TDDFT are qualitatively similar in that they both exhibit two minima corresponding to the proton bonded to the oxygen in one case and the nitrogen in the other. These two surfaces are qualitatively different, however, along the dihedral angle. For the LR-PCM-TDDFT  $\pi\pi^*$  potential energy surface, the **D** and **A** minima are located at smaller dihedral angles ( $\theta = 15^\circ$  and  $22^\circ$ , respectively) than the angle of  $\theta = 34^\circ$  for the ground-state equilibrium geometry. For the SS-PCM-TDDFT  $\pi\pi^*$  potential energy surface, the **D** and **A** minima are located at a larger dihedral angle ( $\theta \approx 94^\circ$ ), where the magnitude of the dipole moment of the  $\pi\pi^*$  state is  $\sim 32$  D. In addition, the SS-PCM-TDDFT rigid scan depicted in Figure S17 (Supporting Information) exhibits a barrierless pathway from the FC geometry to the **A** geometry, suggesting that relaxation of the other solute degrees of freedom is not necessary at this level of theory. Although SS-PCM-TDDFT is typically considered to be a refinement to LR-PCM-TDDFT, we cannot exclude the possibility that SS-PCM-TDDFT might overestimate the solvent stabilization of the  $\pi\pi^*$  state as  $\theta$  is increased toward  $90^\circ$ , where the magnitude of the dipole moment becomes larger. Further studies are required to understand the basis for the qualitative differences between the LR-PCM-TDDFT and SS-PCM-TDDFT  $\pi\pi^*$  potential energy surfaces along the dihedral angles. Our conclusions regarding the character of the relevant electronic states, however, are not influenced by these differences.

**3.3. Qualitative Connection to Dynamics.** As mentioned earlier, the femtosecond transient absorption spectra at early times provided evidence of two distinct spectroscopically accessible low-lying states. Based on the experimental data, the lower and upper states were denoted ICT-EPT and ICT, corresponding to concerted electron–proton transfer and electron transfer alone, respectively. In the present work, we found that these two states correspond to the following: (1) the  $\pi\pi^*$  state with charge-transfer character and one or two minima, where the lowest-energy minimum corresponds to the proton transferred to the base, and (2) the  $n\pi^*$  state without significant charge-transfer character and with only a single minimum close to the FC geometry. On the basis of the femtosecond transient absorption spectra obtained 1 ps following excitation, the higher-energy excitation (355 nm) appears to populate both states, whereas the lower-energy excitation (388 nm) appears to populate only the lower state. This observation suggests that a facile nonadiabatic transition from the ICT to the ICT-EPT state is involved in the relaxation process following the higher-energy excitation. Note that the experiments also provided evidence for intersystem crossing to a triplet state,<sup>20</sup> but we are considering only the singlet-state surfaces relevant to the fast dynamics immediately following photoexcitation.

Figure 7 depicts the potential energy curves along the dihedral angle  $\theta$  for the  $S_1$  and  $S_2$  states of the  $p$ -

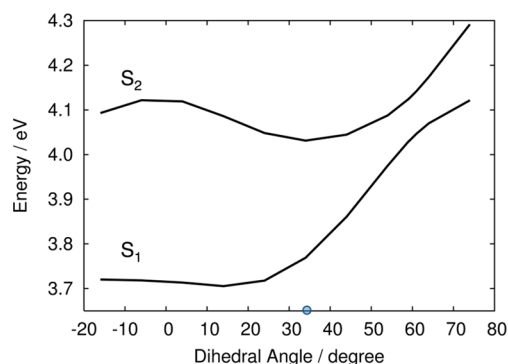


**Figure 7.** Potential energy curves of the  $S_1$  state ( $\pi\pi^*$  state at the FC geometry) and the  $S_2$  state ( $n\pi^*$  state at the FC geometry) for the *p*-nitrophenylphenol–methylamine complex in solution. These curves were generated by changing only the dihedral angle  $\theta$  with all other internal coordinates fixed to the values at the FC geometry, which is identified on the  $x$  axis by the shaded circle. The excited-state energies were calculated with the equilibrium LR-PCM TDDFT/CAM-B3LYP/6-31G(d) method. An avoided crossing between  $S_1$  and  $S_2$  is located at  $\theta \approx 60^\circ$ . For  $\theta$  values greater than the value at the avoided crossing,  $S_1$  and  $S_2$  correspond to the  $n\pi^*$  and  $\pi\pi^*$  states, respectively. The energies are given relative to the ground-state energy at the FC geometry. See Figure S20 (Supporting Information) for the analogous figure generated with  $\omega$ B97XD/6-31G(d) and Figures S21 and S22 (Supporting Information) for the analogous figures generated with the 6-31+G(d,p) basis set.

nitrophenylphenol–methylamine complex in solution calculated with the equilibrium LR-PCM-TDDFT/CAM-B3LYP method. The shaded circle at  $\theta = 34^\circ$  denotes the FC point, from which rigid torsion around the bridging bond is applied to generate the curves. Only the internal dihedral angle  $\theta$  is changed for these calculations, and all other nuclear coordinates remain at the values for the ground-state equilibrium geometry. Similar results were obtained using the  $\omega$ B97XD functional, as shown in Figure S20 (Supporting Information).

Based on the transient absorption spectra,<sup>20</sup> a conical intersection between the  $S_1$  and  $S_2$  states is expected to be located close to the FC geometry. Figure 7 suggests the presence of an avoided crossing between  $S_1$  and  $S_2$  at  $\theta \approx 60^\circ$  with an energy higher than that of the FC point on  $S_2$  by less than 0.1 eV. A more rigorous study that locates and characterizes the conical intersections and investigates the associated nonadiabatic molecular dynamics would be necessary to obtain information about the excited-state dynamics and relaxation processes following photoexcitation for this system.

#### 4. CONCLUSIONS

In this article, the low-lying singlet states of the *p*-nitrophenylphenol–methylamine hydrogen-bonded complex in 1,2-dichloroethane were investigated using TDDFT and ab initio methods in conjunction with PCM solvation. The two singlet excited states that were probed experimentally with transient absorption spectroscopy were identified and characterized computationally. The calculations suggest that the  $\pi\pi^*$  state, which is the  $S_1$  state at the FC geometry, corresponds to the state denoted ICT-EPT in the experimental analysis, whereas the  $n\pi^*$  state, which is the  $S_2$  state at the FC geometry, likely corresponds to the state denoted ICT in the experimental analysis.

According to the calculations, the  $\pi\pi^*$  potential energy surface has two minima corresponding to the proton bonded to

the oxygen donor and to the nitrogen acceptor, separated by a very low barrier, and the lowest-energy minimum corresponds to the proton transferred to the base. At certain levels of theory, only the minimum associated with the transferred proton is observed. These characteristics are consistent with the assignment of EPT character to this state. Moreover, the calculated dipole moment of this excited state is substantially larger than that of the ground state, and the bond length patterns of the  $\pi\pi^*$  state minimum geometries are quinoidal, as in the ICT states of other similar molecules. Finally, the electronic density on the amine base changes upon excitation to this state, indicative of the shifting of electronic density from the O–H bond to the N–H bond that is associated with EPT. In combination, these observations are consistent with the previous assignment of ICT-EPT character to this state.

In contrast, the  $n\pi^*$  potential energy surface has only a single minimum corresponding to the proton bonded to the oxygen, and the geometry associated with this minimum is similar to the FC geometry except for localized changes near the nitro group. Furthermore, the calculated dipole moment of this excited state is similar to that of the ground state, suggesting that this state does not have significant ICT character. Note that this state might not be associated with the higher excited state probed experimentally, although no other singlet states that were close in energy with at least some oscillator strength were observed in the calculations. Thus, we tentatively assign this  $n\pi^*$  state to the state that was denoted ICT in the experimental analysis.

The calculations also provided evidence of an avoided crossing between the  $S_1$  state (the  $\pi\pi^*$  state at the FC geometry) and the  $S_2$  state (the  $n\pi^*$  state at the FC geometry) located energetically close to the FC point, suggesting the proximity of a conical intersection and thus an ultrafast relaxation pathway from the  $n\pi^*$  state to the  $\pi\pi^*$  state. This observation is consistent with the transient absorption spectra. In the present work, we have not considered intersystem crossing to a triplet state, which was also observed experimentally. Moreover, we have not calculated vibrational spectra of the excited electronic states. In ref 20, the coherent Raman spectra were interpreted to indicate the formation of a highly elongated N–H bond directly upon photoexcitation, consistent with an optically induced EPT process.

The direct comparison of the computational studies to the experimental transient absorption spectra would require the simulation of the nonequilibrium solute and solvent dynamics following photoexcitation. We have developed methodology to simulate the nonadiabatic dynamics of photoinduced PCET processes using either implicit<sup>46,47</sup> or explicit<sup>48</sup> solvent. For the implicit solvent treatment, the solvent dynamics is described in terms of two collective solvent coordinates associated with electron and proton transfer. For the explicit solvent treatment, the solute is immersed in a bath of explicit solvent molecules, and the multidimensional potential energy surfaces are calculated “on the fly” during the molecular dynamics. In both cases, the transferring proton is treated quantum mechanically, and an ensemble of surface hopping trajectories is propagated on electron–proton vibronic surfaces. Accurate nonadiabatic dynamics simulations would require the location and characterization of the relevant conical intersections. These types of simulations could provide information about the relaxation pathways on the  $\pi\pi^*$  and  $n\pi^*$  electronic surfaces, as well as nonadiabatic transitions between these two states. Future work will be directed toward these goals.



## ■ ASSOCIATED CONTENT

## ■ Supporting Information

Orbitals, geometries, excitation energies, and potential energy surfaces calculated at various levels of theory, including different functionals and basis sets. This material is available free of charge via the Internet at <http://pubs.acs.org>.

## ■ AUTHOR INFORMATION

## Corresponding Author

\*E-mail: [shs3@illinois.edu](mailto:shs3@illinois.edu).

## Notes

The authors declare no competing financial interest.

## ■ ACKNOWLEDGMENTS

We gratefully acknowledge funding from AFOSR Grant FA9550-10-1-0081. B.H.S. acknowledges Samer Gozem and Prof. Massimo Olivucci for assistance with the MOLCAS calculations. The orbital and density isosurfaces were generated using Molekel.<sup>49</sup>

## ■ REFERENCES

- (1) Hoganson, C. W.; Babcock, G. T. *Science* **1997**, *277*, 1953–1956.
- (2) Alstrum-Acevedo, J. H.; Brennaman, M. K.; Meyer, T. J. *Inorg. Chem.* **2005**, *44*, 6802–6827.
- (3) Gust, D.; Moore, T. A.; Moore, A. L. *Acc. Chem. Res.* **2009**, *42*, 1890–1898.
- (4) Magnuson, A.; Anderlund, M.; Johansson, O.; Lindblad, P.; Lomoth, R.; Polivka, T.; Ott, S.; Stensjö, K.; Styring, S.; Sundström, V.; Hammarström, L. *Acc. Chem. Res.* **2009**, *42*, 1899–1909.
- (5) Hammarström, L.; Hammes-Schiffer, S. *Acc. Chem. Res.* **2009**, *42*, 1859–1860.
- (6) Dempsey, J. L.; Brunschwig, B. S.; Winkler, J. R.; Gray, H. B. *Acc. Chem. Res.* **2009**, *42*, 1995–2004.
- (7) DuBois, D. L.; Bullock, R. M. *Eur. J. Inorg. Chem.* **2011**, *2011*, 1017–1027.
- (8) Sobolewski, A. L.; Domcke, W.; Hättig, C. *Proc. Natl. Acad. Sci. U.S.A.* **2005**, *102*, 17903–17906.
- (9) de La Harpe, K.; Crespo-Hernández, C. E.; Kohler, B. *J. Am. Chem. Soc.* **2009**, *131*, 17557–17559.
- (10) Middleton, C. T.; de La Harpe, K.; Su, C.; Law, Y. K.; Crespo-Hernández, C. E.; Kohler, B. *Annu. Rev. Phys. Chem.* **2009**, *60*, 217–239.
- (11) Stubbe, J.; Nocera, D. G.; Yee, C. S.; Chang, M. C. Y. *Chem. Rev.* **2003**, *103*, 2167–2202.
- (12) Knapp, M. J.; Rickert, K.; Klinman, J. P. *J. Am. Chem. Soc.* **2002**, *124*, 3865–3874.
- (13) Hammes-Schiffer, S. *Energy Environ. Sci.* **2012**, *5*, 7696–7703.
- (14) Sjödin, M.; Styring, S.; Åkermarck, B.; Sun, L.; Hammarström, L. *J. Am. Chem. Soc.* **2000**, *122*, 3932–3936.
- (15) Sjödin, M.; Ghanem, R.; Polivka, T.; Pan, J.; Styring, S.; Sun, L.; Sundström, V.; Hammarström, L. *Phys. Chem. Chem. Phys.* **2004**, *6*, 4851–4858.
- (16) Reece, S. Y.; Nocera, D. G. *J. Am. Chem. Soc.* **2005**, *127*, 9448–9458.
- (17) Concepcion, J. J.; Brennaman, M. K.; Deyton, J. R.; Lebedeva, N. V.; Forbes, M. D. E.; Papanikolas, J. M.; Meyer, T. J. *J. Am. Chem. Soc.* **2007**, *129*, 6968–6969.
- (18) Irebo, T.; Reece, S. Y.; Sjödin, M.; Nocera, D. G.; Hammarström, L. *J. Am. Chem. Soc.* **2007**, *129*, 15462–15464.
- (19) Gagliardi, C. J.; Westlake, B. C.; Kent, C. A.; Paul, J. J.; Papanikolas, J. M.; Meyer, T. J. *Coord. Chem. Rev.* **2010**, *254*, 2459–2471.
- (20) Westlake, B. C.; Brennaman, M. K.; Concepcion, J. J.; Paul, J. J.; Bettis, S. E.; Hampton, S. D.; Miller, S. A.; Lebedeva, N. V.; Forbes, M. D. E.; Moran, A. M.; Meyer, T. J.; Papanikolas, J. M. *Proc. Natl. Acad. Sci. U.S.A.* **2011**, *108*, 8554–8558.
- (21) Casida, M. E. Time-Dependent Density Functional Response Theory for Molecules. In *Recent Advances in Density Functional Methods*; Chong, D. P., Ed.; World Scientific: Singapore, 1995; Part I, p 155.
- (22) Tomasi, J.; Mennucci, B.; Cammi, R. *Chem. Rev.* **2005**, *105*, 2999–3094.
- (23) Levine, B. G.; Ko, C.; Quenneville, J.; Martinez, T. J. *Mol. Phys.* **2006**, *104*, 1039–1051.
- (24) Yanai, T.; Tew, D. P.; Handy, N. C. *Chem. Phys. Lett.* **2004**, *393*, 51–57.
- (25) Vydrov, O. A.; Heyd, J.; Krukau, A. V.; Scuseria, G. E. *J. Chem. Phys.* **2006**, *125*, 074106–074109.
- (26) Vydrov, O. A.; Scuseria, G. E. *J. Chem. Phys.* **2006**, *125*, 234109–234109.
- (27) Henderson, T. M.; Janesko, B. G.; Scuseria, G. E. *J. Chem. Phys.* **2008**, *128*, 194105–194109.
- (28) Chai, J.-D.; Head-Gordon, M. *Phys. Chem. Chem. Phys.* **2008**, *10*, 6615–6620.
- (29) Koch, H.; Jørgensen, P. *J. Chem. Phys.* **1990**, *93*, 3333–3344.
- (30) Stanton, J. F.; Bartlett, R. J. *J. Chem. Phys.* **1993**, *98*, 7029–7039.
- (31) Head-Gordon, M.; Rico, R. J.; Oumi, M.; Lee, T. J. *Chem. Phys. Lett.* **1994**, *219*, 21–29.
- (32) Andersson, K.; Malmqvist, P.-Å.; Roos, B. O. *J. Chem. Phys.* **1992**, *96*, 1218–1226.
- (33) Frisch, M. J.; Trucks, G. W.; Schlegel, H. B.; Scuseria, G. E.; Robb, M. A.; Cheeseman, J. R.; Scalmani, G.; Barone, V.; Mennucci, B.; Petersson, G. A.; Nakatsuji, H.; Caricato, M.; Li, X.; Hratchian, H. P.; Izmaylov, A. F.; Bloino, J.; Zheng, G.; Sonnenberg, J. L.; Hada, M.; Ehara, M.; Toyota, K.; Fukuda, R.; Hasegawa, J.; Ishida, M.; Nakajima, T.; Honda, Y.; Kitao, O.; Nakai, H.; Vreven, T.; Montgomery, J. A., Jr.; Peralta, J. E.; Ogliaro, F.; Bearpark, M.; Heyd, J. J.; Brothers, E.; Kudin, K. N.; Staroverov, V. N.; Kobayashi, R.; Normand, J.; Raghavachari, K.; Rendell, A.; Burant, J. C.; Iyengar, S. S.; Tomasi, J.; Cossi, M.; Rega, N.; Millam, J. M.; Klene, M.; Knox, J. E.; Cross, J. B.; Bakken, V.; Adamo, C.; Jaramillo, J.; Gomperts, R. E.; Stratmann, O.; Yazyev, A. J.; Austin, R.; Cammi, C.; Pomelli, J. W.; Ochterski, R.; Martin, R. L.; Morokuma, K.; Zakrzewski, V. G.; Voth, G. A.; Salvador, P.; Dannenberg, J. J.; Dapprich, S.; Daniels, A. D.; Farkas, O.; Foresman, J. B.; Ortiz, J. V.; Cioslowski, J.; Fox, D. J. *Gaussian 09*, revision B.1; Gaussian, Inc.: Wallingford, CT, 2009.
- (34) Aquilante, F.; De Vico, L.; Ferré, N.; Ghigo, G.; Malmqvist, P.-Å.; Neogrády, P.; Pedersen, T. B.; Pitoňák, M.; Reiher, M.; Roos, B. O.; Serrano-Andrés, L.; Urban, M.; Veryazov, V.; Lindh, R. *J. Comput. Chem.* **2010**, *31*, 224–247.
- (35) Cossi, M.; Barone, V. *J. Chem. Phys.* **2001**, *115*, 4708–4717.
- (36) Improta, R.; Barone, V.; Scalmani, G.; Frisch, M. J. *J. Chem. Phys.* **2006**, *125*, 054103–054109.
- (37) Improta, R.; Scalmani, G.; Frisch, M. J.; Barone, V. *J. Chem. Phys.* **2007**, *127*, 074504–074509.
- (38) Santoro, F.; Improta, R.; Lami, A.; Bloino, J.; Barone, V. *J. Chem. Phys.* **2007**, *126*, 084509–084513.
- (39) Santoro, F.; Lami, A.; Improta, R.; Barone, V. *J. Chem. Phys.* **2007**, *126*, 184102–184111.
- (40) Barone, V.; Improta, R.; Rega, N. *Acc. Chem. Res.* **2008**, *41*, 605–616.
- (41) Scalmani, G.; Frisch, M. J.; Mennucci, B.; Tomasi, J.; Cammi, R.; Barone, V. *J. Chem. Phys.* **2006**, *124*, 094107–094115.
- (42) Finley, J.; Malmqvist, P.-Å.; Roos, B. O.; Serrano-Andrés, L. *Chem. Phys. Lett.* **1998**, *288*, 299–306.
- (43) Hobza, P.; Bludsky, O.; Suhai, S. *Phys. Chem. Chem. Phys.* **1999**, *1*, 3073–3078.
- (44) Koch, W.; Holthausen, M. C. *A Chemist's Guide to Density Functional Theory*, 2nd ed.; Wiley-VCH Verlag GmbH: Weinheim, Germany, 2001.
- (45) Rappoport, D.; Furche, F. *J. Am. Chem. Soc.* **2004**, *126*, 1277–1284.
- (46) Hazra, A.; Soudackov, A. V.; Hammes-Schiffer, S. *J. Phys. Chem. B* **2010**, *114*, 12319–12332.

- (47) Soudackov, A. V.; Hazra, A.; Hammes-Schiffer, S. *J. Chem. Phys.* **2011**, *135*, 144115.
- (48) Auer, B.; Soudackov, A. V.; Hammes-Schiffer, S. *J. Phys. Chem. B* **2012**, *116*, 7695–7708.
- (49) Varetto, U. *Molekel*, v5.4.0; Swiss National Supercomputing Centre: Lugano, Switzerland, 2009.